

Nuclear Quantum Effects and Enzyme Dynamics in Dihydrofolate Reductase Catalysis

Pratul K. Agarwal, Salomon R. Billeter, and Sharon Hammes-Schiffer*

Department of Chemistry, 152 Davey Laboratory, Pennsylvania State University,
University Park, Pennsylvania 16802

Received: January 18, 2002

Mixed quantum/classical molecular dynamics simulations of the hydride transfer reaction catalyzed by dihydrofolate reductase are presented. The nuclear quantum effects such as zero point energy and hydrogen tunneling, as well as the motion of the entire solvated enzyme, are included during the generation of the free energy profiles and the real-time dynamical trajectories. The calculated deuterium kinetic isotope effect agrees with the experimental value. The simulations elucidate the fundamental nature of the nuclear quantum effects and provide evidence of hydrogen tunneling in the direction along the donor–acceptor axis. The transmission coefficient was found to be 0.80 for hydrogen and 0.85 for deuterium, indicating the significance of dynamical barrier recrossings. Nonadiabatic transitions among the vibrational states were observed but did not strongly affect the transmission coefficient. A study of motions involving residues conserved over 36 diverse species from *Escherichia coli* to human implies that motions of residues both in the active site and distal to the active site impact the free energy of activation and the degree of barrier recrossing. This analysis resulted in the characterization of a network of coupled promoting motions that extends throughout the protein and involves motions spanning femtosecond to millisecond time scales. This type of network has broad implications for protein engineering and drug design.

I. Introduction

The enzyme dihydrofolate reductase (DHFR) is required for normal folate metabolism in prokaryotes and eukaryotes. This enzyme catalyzes the reduction of 7,8-dihydrofolate (DHF) to 5,6,7,8-tetrahydrofolate (THF) using nicotinamide adenine dinucleotide phosphate (NADPH) as a coenzyme.¹ Specifically, the pro-*R* hydride of NADPH is transferred to the C6 of the pterin substrate with concurrent protonation at the N5 position. Since this reaction is essential for the maintenance of tetrahydrofolate levels needed to support the biosynthesis of purines, pyrimidines, and amino acids, DHFR has been fostered as a pharmacological target.

As a result of its importance, the mechanism of DHFR has been investigated extensively. Kinetic studies of *Escherichia coli* DHFR have been used to determine the entire kinetic mechanism for DHFR.^{1,2} This mechanism correctly predicts the steady-state kinetic parameters as a function of substrate and cofactor concentrations and pH. These kinetic studies have been applied to single and multiple mutants,^{3,4} as well as to the wild-type enzyme. The mechanism of DHFR has also been studied with *ab initio*, quantum mechanical/molecular mechanical, and free energy perturbation methods.^{5–7} These calculations have provided insight into the hydride transfer step and the active site protonation states and pathways.

In addition to such mechanistic studies, the structure and dynamics of DHFR have been investigated both experimentally and theoretically. Three-dimensional X-ray crystallographic structures have been determined for *E. coli* DHFR in numerous substrate, cofactor, and inhibitor complexes.⁸ (See Figure 1.) These structures indicate that the surface loop formed by residues 9–24 (denoted the Met-20 loop) adopts three different

conformations (denoted closed, occluded, and open) during the catalytic cycle. When the DHFR substrate and NADPH coenzyme are bound, the closed conformation is adopted. This closed conformation is stabilized by hydrogen bonding interactions between the Met-20 loop and the βF – βG loop (residues 117–131). Further insight into the changes in backbone dynamics during the catalytic cycle has been provided by NMR relaxation techniques.^{9,10} NMR experiments on three different DHFR complexes suggest that the binding of the substrate and coenzyme alters the motion of the enzyme in regions far from the binding sites (including the Met-20 and βF – βG loops), as well as in the active site.¹⁰ Additional support for the connection between enzyme motion and catalysis in DHFR has arisen from classical molecular dynamics simulations on three different DHFR complexes.¹¹ In these simulations, strong correlated and anticorrelated side chain motions involving spatially distinct protein regions (again including the Met-20 and βF – βG loops) were observed for the complex with DHF but not for the complexes with THF. Finally, coupling between distal regions of the enzyme is suggested by the nonadditivity effects¹² observed for double mutations in DHFR.^{3,4}

Recently, in collaboration with Benkovic and co-workers, we identified a network of coupled promoting motions in DHFR using a combination of genomic analysis, kinetic measurements of multiple mutations, and mixed quantum/classical molecular dynamics simulations.¹³ Here, promoting motions refer to systematic changes of thermally averaged geometrical properties along a collective reaction coordinate (i.e., as the reaction evolves from the reactant to the transition state). These data were obtained from a series of equilibrium simulations performed with a biasing potential that allowed sufficient sampling of the entire reaction coordinate. On the basis of experimental kinetic measurements of hydride transfer in DHFR, the changes in average geometrical properties between the reactant and the

* To whom correspondence should be addressed. E-mail: shs@chem.psu.edu.

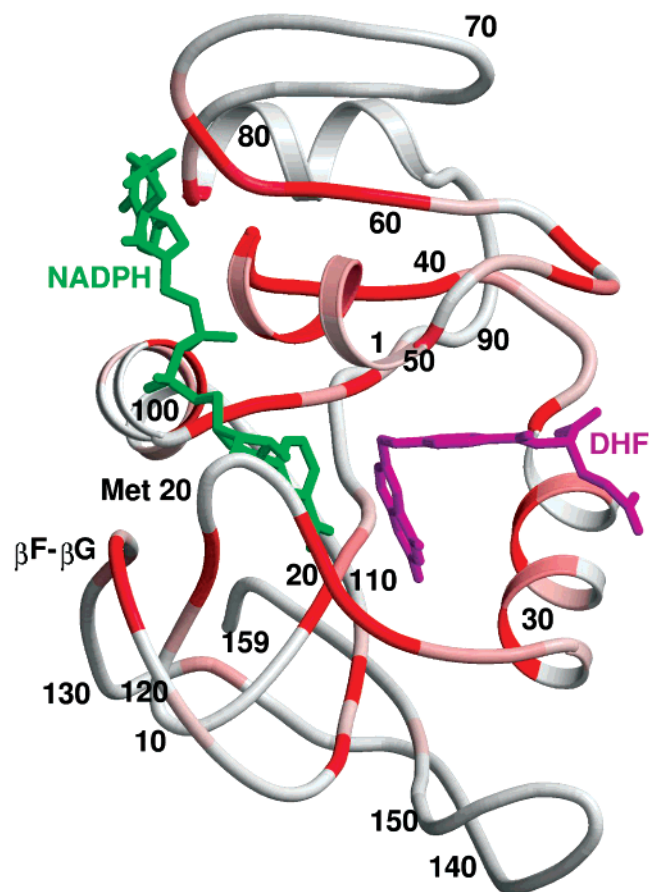
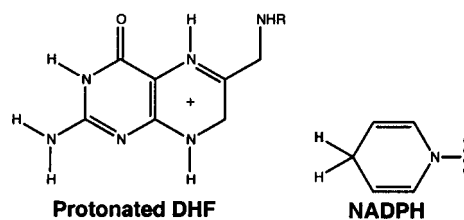


Figure 1. Three-dimensional structure of *E. coli* DHFR.⁸ The Met-20 and βF - βG loops, as well as the DHF substrate and NADPH coenzyme, are indicated. As in ref 13, the residues conserved across numerous species from *E. coli* to human are indicated by a gradient color scheme (grey to red, where red is the most conserved). The details of this genomic analysis are given in ref 13. Residue numbers are indicated periodically for reference.

transition state were determined to occur on the millisecond time scale. The majority of distances monitored did not exhibit systematic changes along the collective reaction coordinate, and many of the motions that did exhibit systematic changes were highly conserved across 36 diverse species of DHFR from *E. coli* to human. Most importantly, the coupled promoting motions in this network were found on the exterior of the enzyme as well as in the active site.

In this paper, we utilize a hybrid approach^{14,15} to investigate the dynamical aspects of this reaction and the nature of the nuclear quantum effects. In this hybrid approach, the free energy profile is generated as a function of a collective reaction coordinate and is used to calculate the transition state theory rate constant. In addition, real-time dynamical trajectories are initiated at the transition state and propagated backward and forward in time to calculate the transmission coefficient, which accounts for dynamical barrier recrossings. Thus, this approach distinguishes between thermally averaged enzyme motions that impact the activation free energy barrier and dynamical motions that impact the degree of barrier recrossing. The nuclear quantum effects such as zero point motion and hydrogen tunneling are incorporated into the free energy profiles and dynamical trajectories by representing the transferring hydrogen nucleus as a three-dimensional wave function. Moreover, the motion of the entire solvated enzyme is included during the generation of the free energy profiles and the propagation of the dynamical trajectories. The application of this hybrid

State 1



State 2

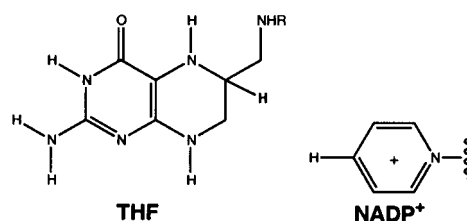


Figure 2. Two EVB states used to describe hydride transfer in DHFR.

approach to DHFR provides insight into the fundamental nature of nuclear quantum effects and the physical basis for dynamical barrier recrossings. It also provides a more complete characterization of the network of coupled promoting motions in DHFR.

II. Methods

The system used in our DHFR calculations contains the protein, an NADPH cofactor, a protonated DHFR substrate, and 4122 water molecules in a truncated octahedral periodic box with a distance of 66.61 Å between opposing square faces. The initial coordinates were obtained from a crystal structure of *E. coli* DHFR complexed with NADPH⁺ and folate (PDB code 1rx2).⁸ In this crystal structure, the Met20 loop is in the closed configuration, which is thought to be the active form for the hydride transfer reaction. The reaction studied is the transfer of the pro-*R* hydrogen on the donor carbon of NADPH to the acceptor carbon of the protonated DHF.

A. EVB Potential. The electronic ground state potential energy surface is determined with an empirical valence bond (EVB) potential¹⁶ based on the two VB structures shown in Figure 2. In VB state 1, the hydride is bonded to its donor carbon, whereas in VB state 2, the hydride is bonded to its acceptor carbon. The diagonal elements of the 2×2 EVB Hamiltonian are described by the GROMOS force field 43A1 with modifications described below, while the off-diagonal element is assumed to be the constant V_{12} .

The standard GROMOS charges were used for the NADPH/NADP⁺ and THF. The charges on the pterin ring of the protonated DHF were assigned by modifying the charges on THF based on similar functional groups in the 43A1 force field.¹⁷ In contrast to the united-atom GROMOS force field, the hydrogen atoms bound to the donor and acceptor carbon atoms are treated explicitly. The protonation states for residues with polar side chains were determined at a pH of 7.0. The protonation state of the His residues was determined by the examination of the hydrogen bonding structures: His-45, 124, and 149 have a proton on ND1, whereas His-114 and 141 have a proton on NE2. The protonated form was used for both Cys residues.

The bond between the transferring hydride and the donor (or acceptor) carbon atom for VB state 1 (or 2) is described by a

Morse potential:

$$V_{\text{Morse}}(R_{\text{CH}}) = D_e(1 - e^{-\alpha(R_{\text{CH}} - R_e)})^2 \quad (1)$$

where R_{CH} is the distance between the hydride and the bonded donor or acceptor carbon atom. The parameters α for the substrate and coenzyme were obtained from electronic structure calculations of the C–H bond frequencies for 6-methyl-pterin and 1-methyl-1,4-dihydronicotinamide, respectively, at the RHF/6-31G*/B3LYP level with a scaling factor of 0.9614.¹⁸ (These calculations were performed with the Gaussian 98 program.¹⁹) The parameter D_e was obtained from experimental dissociation energies,²⁰ and the parameter R_e was obtained from the equilibrium C–H bond length used in the GROMOS force field.¹⁷ The values of these parameters are $\alpha = 1.785 \text{ \AA}^{-1}$, $D_e = 103 \text{ kcal/mol}$, and $R_e = 1.09 \text{ \AA}$ for the bond between the donor carbon and the hydride, and $\alpha = 1.758 \text{ \AA}^{-1}$, $D_e = 103 \text{ kcal/mol}$, and $R_e = 1.09 \text{ \AA}$ for the bond between the acceptor carbon and the hydride. Although the GROMOS functional form of angular interactions²¹ was retained for the classical molecular dynamics calculations, the bending angle interactions were changed to harmonic¹⁴ for the transferring hydride in all mixed quantum/classical molecular dynamics calculations to prevent artifacts in higher energy regions. All other bonds involving hydrogen atoms were constrained.

The coupling between the two VB states (i.e., the off-diagonal matrix element) is assumed to be a constant V_{12} , and a constant energy adjustment Δ_{12} is included in V_{22} . Both V_{12} and Δ_{12} have been chosen to ensure that the quantum free energy profile for the reaction reproduces the experimental free energies of reaction and activation. The maximum forward and reverse rates for hydride transfer were measured to be 950 s^{-1} and 0.55 s^{-1} , respectively.² This leads to free energies of activation and reaction of 13.4 kcal/mol and -4.4 kcal/mol , respectively. The resulting values for these parameters are $V_{12} = 30.0 \text{ kcal/mol}$ and $\Delta_{12} = 58.8 \text{ kcal/mol}$. [Upon further parametrization, we found that the value of Δ_{12} increased somewhat ($< 1 \text{ kcal/mol}$), but this does not significantly influence the quantities reported in this paper.] Note that this fitting procedure does not include the effects of the transmission coefficient, which will decrease the calculated rate relative to the experimentally determined rate. Although an iterative procedure could be implemented to include these effects, this factor is not expected to alter the qualitative results.

The electrostatic and Lennard-Jones interactions are treated consistently with the GROMOS force field. The cutoff radius for nonbonded interactions is 14 \AA , and the nonbonded interactions between 8 and 14 \AA are calculated only every five molecular dynamics steps, along with updating the charge-group based nonbonded interactions pair list. Outside the sphere of radius 14 \AA , the electrostatics are represented by a reaction field with a relative dielectric constant of 54 and a zero inverse Debye screening length.

B. Nuclear Quantum Effects. Numerous methods have been developed for the inclusion of nuclear quantum effects in simulations of enzyme reactions.^{22–36} In this paper, the nuclear quantum effects of the transferring hydrogen are incorporated into our simulations by representing this nucleus as a three-dimensional vibrational wave function. For this purpose, we use a mixed quantum/classical description of the nuclei, in which the transferring hydrogen nucleus with coordinate \mathbf{r} is treated quantum mechanically, whereas the remaining nuclei with coordinates \mathbf{R} are treated classically. The adiabatic vibrational wave functions for the transferring hydrogen are calculated for fixed classical coordinates \mathbf{R} by solving the time-independent

Schrödinger equation:

$$[T_{\text{H}} + V_{\text{el0}}(\mathbf{r}, \mathbf{R})]\Phi_j(\mathbf{r}; \mathbf{R}) = \epsilon_j(\mathbf{R})\Phi_j(\mathbf{r}; \mathbf{R}) \quad (2)$$

where T_{H} is the kinetic energy of the transferring hydrogen and $V_{\text{el0}}(\mathbf{r}, \mathbf{R})$ is the potential energy of the electronic ground state. In this paper, we include the nonadiabatic effects from the excited vibrational states to allow an accurate calculation of the hydrogen quantum effects. Thus, eq 2 is solved for a range of states j .

As will be described below, eq 2 must be solved for each configuration of the classical nuclei during the generation of the free energy profiles and during the dynamical calculation of the transmission coefficient. This calculation is facilitated through use of the state-averaged Fourier grid Hamiltonian multiconfigurational self-consistent-field (FGH-MCSCF) method for calculating multidimensional hydrogen vibrational wave functions³⁷ and a partial multidimensional grid generation method to decrease the number of potential energy calculations.³⁸ This approach accurately describes ground and excited state hydrogen vibrational wave functions in a computationally practical manner. For the calculations presented in this paper, the transferring hydride is represented on a three-dimensional cubic grid centered between the donor and acceptor carbon atoms. The length of each side of the cubic grid is 5.82 \AA , with 64 grid points per spatial dimension. For the FGH-MCSCF calculations, the active space is spanned by five one-dimensional states per dimension, and the wave function is calculated by state-averaging over the lowest four multiconfigurational states. A cutoff of 94.1 kcal/mol for the potential energy is used for the partial multidimensional grid generation.

C. Free Energy Profiles. To calculate the transition state theory rate constant, the free energy profile must be calculated. The transition state theory rate constant is³⁹

$$k_{\text{TST}} = \frac{k_{\text{B}}T}{h} e^{-\Delta G^\ddagger/k_{\text{B}}T} \quad (3)$$

where ΔG^\ddagger is the free energy barrier for the reaction and k_{B} is Boltzmann's constant. Since the hydride transfer reaction involves a free energy barrier that is significantly larger than the thermal energy, the free energy profiles were obtained from molecular dynamics simulations governed by the mapping potential¹⁶

$$V_{\text{map}}(\mathbf{r}, \mathbf{R}; \lambda) = (1 - \lambda)V_{11}(\mathbf{r}, \mathbf{R}) + \lambda V_{22}(\mathbf{r}, \mathbf{R}) \quad (4)$$

where V_{11} and V_{22} are the diagonal elements of the EVB Hamiltonian. As the parameter λ is varied from zero to unity, the reaction progresses from the reactant VB state 1 to the product VB state 2. In this paper, we calculate both the classical free energy profile, corresponding to the classical treatment of the transferring hydrogen nucleus, and the quantum free energy profile, corresponding to the quantum mechanical treatment of the transferring hydrogen nucleus. A comparison of the classical and quantum free energy profiles provides an indication of the significance of nuclear quantum effects.

The free energy profiles are calculated as functions of a collective reaction coordinate analogous to the solvent coordinate used in standard Marcus theory for electron transfer reactions.^{40–43} When the transferring hydrogen is treated classically, this collective reaction coordinate is defined as

$$\Lambda(\mathbf{r}, \mathbf{R}) = V_{22}(\mathbf{r}, \mathbf{R}) - V_{11}(\mathbf{r}, \mathbf{R}) \quad (5)$$

In this case, the reaction coordinate depends on both \mathbf{r} and \mathbf{R} . When the transferring hydrogen is treated quantum mechanically, the reaction coordinate should not be a function of the quantum coordinate \mathbf{r} because the classical molecular dynamics samples the configurational space of only the classical coordinates \mathbf{R} . Moreover, the reaction coordinate $\Lambda^{(c)}(\mathbf{r}, \mathbf{R})$ defined in eq 5 does not distinguish between symmetric and asymmetric hydrogen potential energy surfaces (or hydrogen vibrational wave functions), as required in the framework of standard Marcus theory.⁴⁰ Thus, the physically meaningful reaction coordinate when the transferring hydrogen nucleus is treated quantum mechanically is defined as

$$\Lambda^{(q)}(\mathbf{R}) = \langle \Phi_0(\mathbf{r}; \mathbf{R}) | V_{22}(\mathbf{r}, \mathbf{R}) - V_{11}(\mathbf{r}, \mathbf{R}) | \Phi_0(\mathbf{r}; \mathbf{R}) \rangle_{\mathbf{r}} \quad (6)$$

where $\langle \cdots \rangle_{\mathbf{r}}$ indicates integration over the quantum coordinate \mathbf{r} and $\Phi_0(\mathbf{r}; \mathbf{R})$ is the ground state vibrational wave function. Note that, in practice, the classical and quantum reaction coordinates are divided into discrete intervals (i.e., bins) represented by values Λ_n .

The calculation of the classical free energy profile for the electronic ground state potential $V_{\text{el0}}(\mathbf{r}, \mathbf{R})$ consists of three steps.¹⁴ In the first step, the free energy $F_{\text{map}}(\Lambda_n; \lambda_m)$ for the mapping potential along the reaction coordinate $\Lambda^{(c)}(\mathbf{r}, \mathbf{R})$ defined in eq 5 is calculated for each λ_m using a standard binning procedure during molecular dynamics simulations governed by $V_{\text{map}}(\mathbf{r}, \mathbf{R}; \lambda_m)$. In the second step, the relative free energies for the mapping potential corresponding to the same value of Λ_n but different values of λ_m are determined from thermodynamic integration. Note that this procedure avoids the arbitrary translation of the individual segments of the free energy profile corresponding to different values of λ_m . Moreover, the degree of overlap of the neighboring segments provides an indication of the convergence of the calculations. In the third step, the classical free energy $F_{\text{el0}}(\Lambda_n; \lambda_m)$ for the electronic ground state potential $V_{\text{el0}}(\mathbf{r}, \mathbf{R})$ is calculated from the molecular dynamics simulations governed by the mapping potential using a perturbation formula.

The quantum free energy profiles include the vibrationally adiabatic nuclear quantum effects for the transferring hydrogen nucleus. The quantum free energy $F_{\text{el0,nuc0}}(\Lambda_n; \lambda_m)$ associated with the ground state hydrogen vibrational wave function (with energy $\epsilon_0(\mathbf{R})$ given in eq 2) is calculated from the perturbation formula derived in ref 14. Assuming adequate sampling, the use of this perturbation formula is rigorously identical to adiabatic mixed quantum/classical molecular dynamics simulations that include feedback between the quantum and classical subsystems.

Thus, both the classical and quantum free energy profiles are obtained from molecular dynamics simulations governed by the mapping potential $V_{\text{map}}(\mathbf{r}, \mathbf{R}; \lambda)$. These simulations are performed using GROMOS²¹ and a modified FORCE routine. The integration time step is 1 fs, and the constraints are maintained by SHAKE.⁴⁴ Two separate Berendsen thermostats⁴⁵ with relaxation times of 0.1 ps each maintain the temperature of the solute and the water molecules at 300 K. The initial configuration for the reactant state was equilibrated in four steps, gradually releasing the force constant of position restraints to the crystal structure positions⁸ from 100 kcal/(mol Å²) to 50, 25, and 0 kcal/(mol Å²). Each step consisted of a steepest descent geometry optimization followed by 5 ps molecular dynamics. After this initialization, the free energy profiles were generated through a series of different mapping parameters λ_m . For each value of the mapping parameter λ_m (0.0, 0.05, 0.125, 0.25, 0.375, 0.5, 0.625, 0.75, 0.875, 0.95, and 1.0), the final

coordinates from the previous value of λ_m were first optimized, and then the system was equilibrated for 5 ps. The configurations were then equilibrated for another 60 ps, followed by 140 ps of data collection. The energies and energy derivatives of every fifth step have been used for both the thermodynamic integration and the generation of the classical free energy profile. For storage reasons, the coordinates were stored only every 25 steps for the generation of the quantum free energy profile.

D. Dynamical Trajectories. The transition state theory rate constant k_{TST} defined in eq 3 is based on the assumption that the rate is determined by the forward flux through the dividing surface. Thus, transition state theory assumes that each trajectory passes through the dividing surface only one time. In dynamical systems, the environment may cause trajectories to recross the dividing surface. The “exact” rate constant k_{dyn} including dynamical effects may then be expressed as

$$k_{\text{dyn}} = \kappa k_{\text{TST}} \quad (7)$$

where κ is the transmission coefficient that accounts for recrossings of the dividing surface.⁴⁶

In this paper, the dynamical effects for this reaction are calculated by combining the MDQT surface hopping method^{22,23,47} with a reactive flux method for infrequent events.¹⁴ The fundamental principle of MDQT is that an ensemble of trajectories is propagated, and each trajectory moves classically on a single adiabatic surface except for instantaneous transitions among the adiabatic states. The adiabatic states $\Phi_n(\mathbf{r}; \mathbf{R})$ are calculated at each classical molecular dynamics time step by solving eq 2 with the state-averaged FGH-MCSCF method.³⁷ The classical nuclei evolve according to Newton’s classical equations of motion with the effective potential $\epsilon_k(\mathbf{R})$ (defined in eq 2), where k denotes the occupied adiabatic state. The time-dependent wave function describing the quantum nuclei is expanded in a basis of the adiabatic states:

$$\Psi(\mathbf{r}, \mathbf{R}, t) = \sum_{j=0}^{N_{\text{ad}}-1} C_j(t) \Phi_j(\mathbf{r}; \mathbf{R}) \quad (8)$$

and the quantum amplitudes $C_j(t)$ are calculated by integrating the time-dependent Schrödinger equation simultaneously with the classical equations of motion. At each time step, Tully’s “fewest switches” algorithm⁴⁷ is invoked to determine if a quantum transition to another adiabatic state should occur. This algorithm correctly apportions trajectories among the adiabatic states according to the quantum probabilities $|C_j(t)|^2$ with the minimum required number of quantum transitions (neglecting difficulties with classically forbidden transitions).

In standard classical molecular dynamics simulations, κ may be calculated using reactive flux methods for infrequent events.^{39,48–50} In this approach, κ is calculated as the flux-weighted average of a quantity ξ for a canonical ensemble of classical molecular dynamics trajectories started at the dividing surface and integrated backward and forward in time. The quantity ξ corrects for multiple crossings of the dividing surface (i.e., so that all trajectories that originate as reactants and end as products are counted only once, no matter how many times they cross the dividing surface, and all trajectories that go from reactants to reactants, products to products, or products to reactants are not counted at all). In particular, $\xi = 1/\alpha$ for trajectories that have α forward crossings and $\alpha - 1$ backward crossings of the dividing surface, and ξ is zero otherwise.

In the reactive flux method for infrequent events, a flux-weighted canonical ensemble of molecular dynamics trajectories

is started at the dividing surface and integrated backward and forward in time. The use of the standard classical reactive flux approach in conjunction with MDQT is problematic because the probability of nonadiabatic transitions depends on the quantum amplitudes, which depend on the history of the trajectory. Thus, trajectories started at the dividing surface cannot be propagated backward in time with the MDQT method. (Backward propagation requires knowledge of the quantum amplitudes at the dividing surface, which are unavailable.) To surmount this difficulty, we use the method developed by Hammes-Schiffer and Tully for simulating infrequent events in reactions that evolve on multiple potential energy surfaces.⁵¹ In this approach, trajectories are started at the dividing surface and propagated backward in time with a fictitious surface hopping algorithm that does not depend on the quantum amplitudes. The trajectory is then propagated forward in time, retracing the exact same trajectory, integrating the quantum amplitudes and calculating the probabilities for nonadiabatic transitions for each time step using the true surface hopping algorithm. Each trajectory is assigned a weighting that ensures that the overall results are identical to those that would have been obtained with the true surface hopping algorithm.

In the implementation of this reactive flux method for MDQT within the framework of the methodology presented in this paper,¹⁴ the weighted average of a quantity x is

$$\langle x \rangle_w = \frac{\sum_{i=1}^{N_{\text{traj}}} (\dot{\mathbf{R}}_i \cdot \hat{\mathbf{n}}_i) w_i^{\text{can}} w_i^{\text{sh}} x_i}{\sum_{i=1}^{N_{\text{traj}}} (\dot{\mathbf{R}}_i \cdot \hat{\mathbf{n}}_i) w_i^{\text{can}} w_i^{\text{sh}}} \quad (9)$$

The transmission factor κ is then

$$\kappa = \langle \xi \rangle_w \quad (10)$$

Here N_{traj} is the number of trajectories required to represent an ensemble, $\dot{\mathbf{R}}_i$ is the initial velocity vector, and $\hat{\mathbf{n}}_i$ is the unit vector normal to the dividing surface. The weightings w_i^{can} ensure a canonical distribution at the dividing surface. These weightings include both a factor accounting for the generation of the ensemble of initial configurations at the dividing surface with the mapping potential and a factor accounting for a Boltzmann distribution over the vibrational adiabatic states at the dividing surface. The weightings w_i^{sh} ensure the correct surface hopping probabilities for each trajectory within the ensemble. These weightings are obtained from the backward propagation with the fictitious surface hopping algorithm and the subsequent forward propagation over the exact same trajectory while integrating the quantum amplitudes and calculating the probabilities of nonadiabatic transitions for the true surface hopping algorithm. (Note that the quantum amplitudes for the forward propagation are initialized such that the quantum amplitude of the occupied state after the backward propagation is unity.)

For the MDQT simulations, the classical equations of motion are integrated using the velocity Verlet algorithm⁵² with a time step of 0.5 fs, maintaining the constraints with RATTLE.⁵³ Note that no thermostat is used for the MDQT simulations, and therefore, the nonbonded interactions pairlist is not updated. This aspect of the MDQT simulations is not problematic because of the short duration of each MDQT trajectory. To avoid artifacts because of abrupt changes in momentum, the velocities are not reversed after classically forbidden nonadiabatic transitions. The

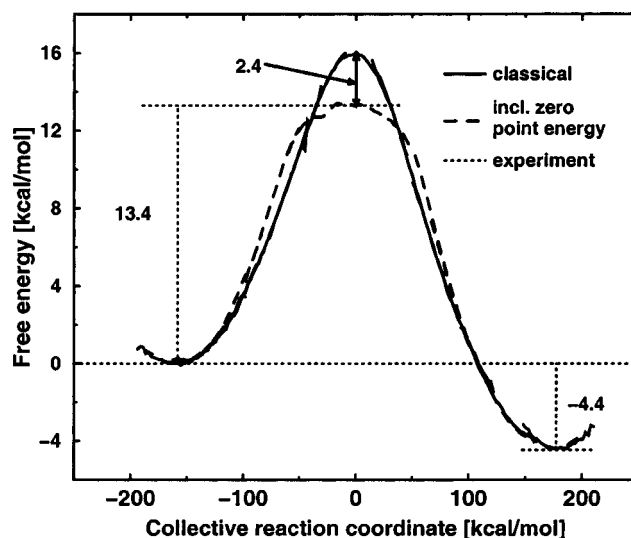


Figure 3. Classical and adiabatic quantum free energy profiles for the hydride transfer reaction as functions of a collective reaction coordinate. The solid line indicates the classical profile, and the dashed line indicates the adiabatic quantum profile (including zero point motion for the transferring hydride). The minimum free energies of the classical and adiabatic quantum profiles are set to zero, and the difference in free energy barriers is indicated. The dotted lines denote experimental values.

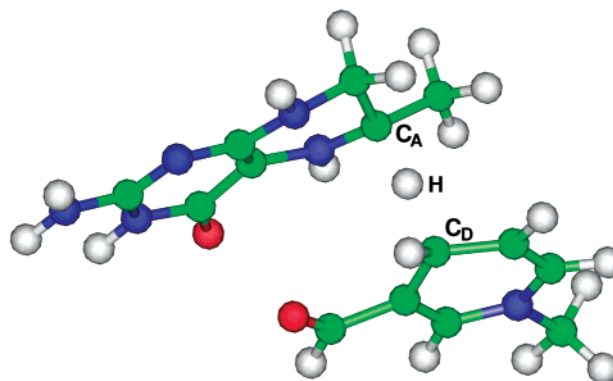


Figure 4. Transition state structure calculated at the RHF/6-31G** level for a model system representing hydride transfer in DHFR. The donor and acceptor carbon atoms and the transferring hydride are indicated. The donor complex is 6-methyl-pterin, and the acceptor complex is 1-methyl-1,4-dihydronicotinamide. The color scheme is as follows: red = oxygen, blue = nitrogen, green = carbon, and white = hydrogen.

dividing surface used for the reactive flux method is defined to be $\Lambda^{(q)}(\mathbf{R}) = 0$. The trajectories are propagated in the forward and backward directions until $|\Lambda^{(q)}(\mathbf{R})| > 125.5$ kcal/mol for twenty sequential time steps. This criterion is designed to indicate that the trajectory is out of the strong coupling region and in either the reactant or the product region.

III. Results

A. EVB Potential. To investigate the accuracy of the EVB potential, we compared relevant geometrical properties obtained from our simulations to an electronic structure calculation of the model system shown in Figure 4. In particular, we compared each specified geometrical property averaged over configurations at the transition state for our hybrid simulations including the entire solvated enzyme to this property at the transition state calculated at the RHF/6-31G** level for the model system. Note that the definition of transition state is fundamentally different

TABLE 1: Comparison of Geometrical Properties^a

property	ab initio ^b	EVB ^c
C _D –C _A distance	2.69	2.73
C _D –H–C _A angle	166	164
DHF ring puckering angle ^d	–31.3	–31.9
NADPH ring puckering angle ^d	10.7	0.01

^a Distances in angstroms and angles in degrees. ^b Determined from the transition state of an RHF/6-31G** calculation for the model system in Figure 4. ^c Determined from averaging over configurations at the transition state ($\Lambda^{(q)}(\mathbf{R}) = 0$) for an EVB mixed quantum/classical molecular dynamics simulation including the entire solvated enzyme.

^d Ring puckering angles are defined in ref 15.

for the EVB mixed quantum/classical molecular dynamics simulations and the standard electronic structure calculation. In the standard electronic structure calculation, the transition state is defined as a first-order saddle point on the potential energy surface. In our hybrid approach, the transition state is defined to occur when the collective reaction coordinate is zero (i.e., when the hydrogen potential is virtually symmetric). The results of the comparison of relevant geometrical properties are given in Table 1. The agreement for the donor–acceptor distance, the donor–hydride–acceptor angle, and the ring puckering angle for the acceptor carbon in the substrate pterin ring is excellent. The ring puckering angle for the donor carbon in the NADPH ring exhibits a discrepancy, which is due to either the inadequacy of a pairwise additive force field in reproducing many-body electronic effects or the impact of the protein environment on this angle in DHFR compared to the simple model system in Figure 4. In any case, this relatively minor effect on the NADPH ring puckering angle is not expected to influence the qualitative results presented in this paper. The overall agreement for these relevant geometrical properties indicates that the EVB potential provides a physically reasonable description of the reacting region.

B. Nuclear Quantum Effects. The free energy profiles for the transfer of a classical and a quantum mechanical hydride nucleus are compared in Figure 3. In this hybrid approach, the zero point motion of the transferring hydride nucleus is included in the adiabatic quantum free energy profile along the collective reaction coordinate through the representation of this nucleus as a three-dimensional wave function. Figure 3 indicates that the nuclear quantum effects decrease the free energy barrier for this reaction by ~ 2.4 kcal/mol. Furthermore, although the shapes of the classical and quantum free energy profiles are very similar in the reactant and product regions, they differ considerably in the transition state region because of the delocalization of the hydride wave function. (Note that the coupling between the EVB surfaces V_{12} and the constant energy adjustment Δ_{12} have been chosen such that the quantum free energy profile reproduces the experimental free energies of activation and reaction.²)

Figure 5 depicts the hydrogen nuclear wave functions corresponding to representative configurations for the reactant, transition state, and product. For the reactant and product, the vibrational wave functions are localized near the donor and acceptor, respectively. For these configurations, the ground state is approximately spherical, whereas the first excited state has one node and is directed approximately perpendicular to the donor–acceptor axis. Although not shown here, the second excited state has one node and is directed approximately perpendicular to the donor–acceptor axis, whereas the third excited state has one node and is directed approximately along the donor–acceptor axis. The weighted average excitation energies for the reactant are 1065, 1190, and 2122 cm^{-1} for the first, second, and third excited states, respectively. The

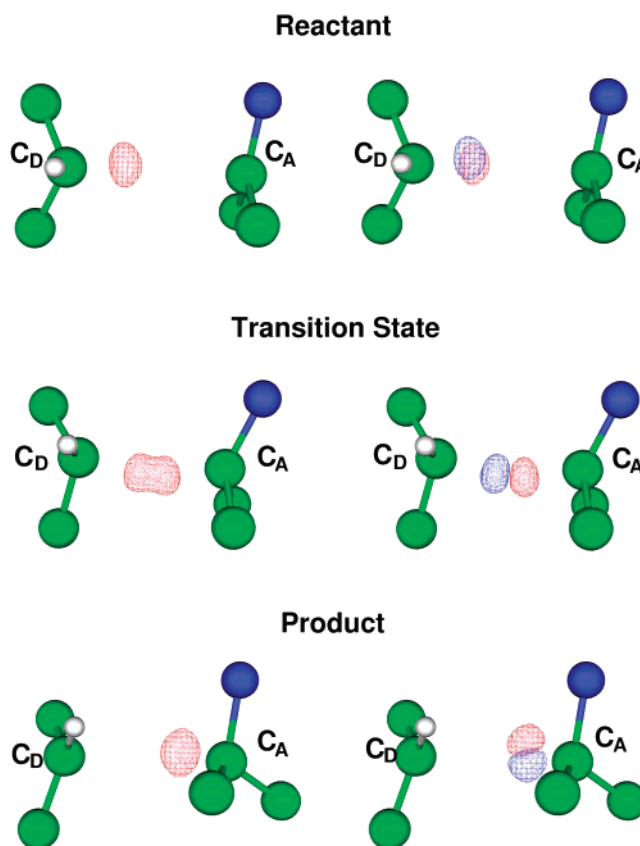


Figure 5. Vibrational wave functions of the transferring hydride for representative configurations. On the donor side, the donor carbon atom and its first neighbors are shown, whereas on the acceptor side, the acceptor carbon atom and its first neighbors are shown. The ground and excited vibrational states are shown on the left and right, respectively.

excitation frequencies for the first and second excited states are similar to the local harmonic frequencies for the bending mode of a typical C–H bond (1400–1500 cm^{-1}).⁵⁴ The excitation frequency for the third excited state is similar to the local harmonic frequency for the stretching mode of a typical C–H bond (2800–2900 cm^{-1}).⁵⁴ Our calculated frequencies are somewhat lower than the typical local harmonic values because of anharmonicities excluded in the construction of the potential, coupling among the modes, and the proximity of other atoms in the system, particularly the acceptor carbon atom. Nevertheless, the calculated frequencies agree qualitatively with the typical values obtained from a local harmonic treatment. For the transition state, the vibrational wave functions are delocalized between the donor and acceptor. In this case, the ground and first excited states are symmetric and antisymmetric wave functions, respectively, directed along the donor–acceptor axis, indicating that this vibrational excitation corresponds approximately to a C–H–C stretching mode along the donor–acceptor axis.

A further analysis of the transition state wave functions provides insight into the fundamental nature of the nuclear quantum effects. The splittings between the lowest two hydrogen vibrational states for observed transition states range from 0.44 to 2.69 kcal/mol, with the weighted average splitting being 0.81 kcal/mol. An analysis of hydrogen tunneling is not straightforward because of the three-dimensional nature of the hydrogen potentials and wave functions. To aid in our analysis, we calculated the one-dimensional hydrogen vibrational wave functions for the one-dimensional potentials projected along the donor–acceptor axis. (This one-dimensional potential was

TABLE 2: Statistics of MDQT Trajectories^a

	hydrogen			deuterium		
# crossings of dividing surface	all	= 1	≥ 2	all	= 1	≥ 2
trajectory productivity	all	prod	non	all	prod	non
number of trajectories in category	357	227	130	327	237	90
transmission coefficient $\langle \xi \rangle_w = \kappa$	0.83	1.00	0.00	0.87	1.00	0.00
$\langle \# \text{ forward crossings} \rangle_w$	1.03	1.00	1.20	1.05	1.00	1.32
$\langle \# \text{ backward crossings} \rangle_w$	0.18	0.00	1.21	0.21	0.00	1.32
$\langle \text{total time of trajectory} \rangle_w$	95.29	94.90	97.45	100.69	99.51	106.8
$\langle \text{time in coupling region} \rangle_w^b$	11.26	10.60	14.95	10.39	10.28	10.96
$\langle \text{total time in state } 1 \rangle_w$	0.13	0.01	0.81	0.73	0.11	3.92
$\langle \text{time in coupling region, state } 1 \rangle_w^b$	0.00	0.00	0.03	0.47	0.02	2.79
$\langle \# \text{ transitions from/into state } 1 \rangle_w$	0.01	0.00	0.05	0.12	0.02	0.65
flux ^c	7.62	8.96	4.38	8.88	9.80	5.46
average weight ^d	1.00	1.11	0.80	1.00	1.09	0.77

^a Trajectories were obtained from 91 configurations with 4 sets of initial velocities per configuration for H and 41 configurations with 8 sets of initial velocities per configuration for D. All trajectories include in this table were initiated in the ground vibrational state at $t = 0$. $\langle \dots \rangle_w$ is defined in eq 9. State 1 refers to the first excited vibrational state. Units are fs for time and nm/ps for flux. ^b The coupling region is defined as $|\Lambda^{(q)}(\mathbf{R})| \leq 62.75$ kcal/mol. ^c Flux = $(\sum_{i=1}^{N_{\text{traj}}} w_i^{\text{can}} w_i^{\text{sh}} \dot{\mathbf{R}}_i \cdot \hat{\mathbf{n}}_i) / (\sum_{i=1}^{N_{\text{traj}}} w_i^{\text{can}} w_i^{\text{sh}})$. ^d Average weight = $\sum_{i=1}^{N_{\text{traj}}} \dot{\mathbf{R}}_i \cdot \hat{\mathbf{n}}_i w_i^{\text{can}} w_i^{\text{sh}} / N_{\text{traj}}$ scaled so that the average weight of all trajectories is unity.

obtained by choosing the lowest value of the potential energy in the plane perpendicular to the donor–acceptor axis for each grid point along this axis.) We found that the splittings between the lowest energy one-dimensional hydrogen vibrational states are similar to the splittings for the lowest energy three-dimensional vibrational states. (The minor differences between the one- and three-dimensional splittings are due to coupling among the dimensions.) For the smallest observed splitting at the transition state, the lowest two one-dimensional vibrational states are both below the one-dimensional barrier. For the largest observed splitting, the lowest two one-dimensional vibrational states are both above the one-dimensional barrier. For the average splitting, the lowest one-dimensional vibrational state is ~ 1.1 kcal/mol below the one-dimensional barrier. Although this simplified analysis neglects coupling among the dimensions, it provides insight into the nature of the nuclear quantum effects. Specifically, this analysis implies that some hydrogen tunneling (i.e., transmittal of probability through a barrier) occurs in the direction along the donor–acceptor axis during the DHFR hydride transfer reaction.

We have calculated the adiabatic quantum free energy profiles for the transfer of hydrogen and deuterium. The free energies of activation for these isotopes are 13.4 and 14.2 kcal/mol, respectively. The difference in the free energy of activation result in a deuterium kinetic isotope effect of $k_{\text{TST}}^{\text{H}}/k_{\text{TST}}^{\text{D}} = 3.4 \pm 0.6$. The experimental deuterium kinetic isotope effect is $k_{\text{exp}}^{\text{H}}/k_{\text{exp}}^{\text{D}} = 3.0 \pm 0.4$.² The agreement of our calculated deuterium isotope effect with the experimental value provides further confirmation of the validity of this model. Note that these calculated kinetic isotope effects do not yet contain nonequilibrium effects such as dynamical barrier recrossings.

C. Transmission Coefficients. The transmission coefficients for hydrogen and deuterium were calculated from an ensemble of dynamical trajectories. The calculated values for hydrogen and deuterium were $\kappa_{\text{H}} = 0.80 \pm 0.03$ and $\kappa_{\text{D}} = 0.85 \pm 0.01$. Inclusion of the transmission coefficients adjusts the transition state theory deuterium kinetic isotope effects to $k_{\text{dyn}}^{\text{H}}/k_{\text{dyn}}^{\text{D}} = 3.2 \pm 0.6$, which agrees even better with the experimental value.

We have performed a detailed analysis of the ensemble of trajectories to determine the physical basis for the calculated transmission coefficients. The results of this analysis are summarized in Table 2. Although we analyzed trajectories started in the vibrational ground and first two excited states, only the results for trajectories started in the vibrational ground state are shown here. (The trajectories started in the excited states

had much smaller weightings because of the Boltzmann factor ensuring a canonical distribution at the dividing surface.)

For hydrogen, 62% of the trajectories are productive with only a single crossing of the dividing surface, whereas the remaining trajectories are nonproductive. Most of the nonproductive trajectories have only a single forward crossing of the dividing surface and recross the dividing surface almost immediately after this forward crossing. This is evident from the average number of forward crossings (1.2, which is close to unity). These data also imply that nonadiabatic transitions are not significant for these trajectories. The recrossings appear to be due to insufficient flux, as indicated by the smaller flux for the nonproductive trajectories (4.38 nm/ps) than for the productive trajectories (8.96 nm/ps). This observation suggests that trajectories with lower flux respond more to the friction of the environment, leading to a higher probability of barrier recrossings.

For deuterium, 72% of the trajectories are productive with only a single crossing of the dividing surface, whereas the remaining trajectories are nonproductive. The larger percentage of productive trajectories with a single crossing for deuterium than for hydrogen leads to a larger transmission coefficient for deuterium. The deuterium trajectories behave qualitatively similar to the hydrogen trajectories. For deuterium, however, slightly more of the nonproductive trajectories have multiple forward crossings of the dividing surface (i.e., the average number of forward crossings is 1.32 for deuterium and 1.20 for hydrogen). Nevertheless, even for deuterium, most of the trajectories exhibiting recrossings are nonproductive with only a single forward crossing of the dividing surface followed quickly by a backward recrossing.

As a result of the smaller splittings between the vibrational states, the deuterium trajectories exhibit more nonadiabatic transitions than the hydrogen trajectories, as indicated by the larger average number of transitions from and into state 1 (0.12 for deuterium and 0.01 for hydrogen). As a result, the deuterium trajectories spend more time in the first excited state than the hydrogen trajectories (0.73 fs versus 0.13 fs), whereas their total times are comparable. Even for deuterium, however, the average time spent in the first excited state is small relative to the average time in the coupling region, implying that the nonadiabatic transitions are not causing significant barrier recrossings because of trapping in the first excited state.

D. Enzyme Motion. This hybrid approach allows us to distinguish between enzyme motions influencing the free energy

of activation and motions influencing the degree of barrier recrossing. The enzyme motions influencing the free energy barrier are determined from the equilibrium adiabatic simulations along the collective reaction coordinate. An analysis of these simulations elucidates systematic changes in thermally averaged geometrical properties as the reaction evolves from the reactant to the transition state to the product. These changes in average geometrical properties occur on the millisecond time scale of the hydride transfer reaction. The individual simulations are propagated for only hundreds of picoseconds, but a series of such simulations are connected along the entire collective reaction coordinate in a way that provides information on the millisecond time scale. (Note that trapping in metastable minima may be problematic for this analysis.) The enzyme motions influencing the degree of barrier recrossing are determined from MDQT reactive flux calculations, where an ensemble of trajectories is initiated at the transition state and propagated backward and forward in time. (The initial configurations at the transition state are obtained from equilibrium simulations with a biasing potential.) These reactive flux calculations provide nonequilibrium, real-time, dynamical information in the region of the transition state, typically on the femtosecond to picosecond time scale. An analysis of the trajectories provides the correlation between geometrical properties at the transition state and the degree of barrier recrossing.

Table 3 provides information about the impact of specified geometrical properties on both the activation free energy barrier and the degree of dynamical barrier recrossing. To determine the motions influencing the activation free energy barrier, we calculated the difference between a thermally averaged geometrical property at the transition state and at the reactant. The ratio of this quantity to the value at the reactant provides the percentage change for this averaged geometrical property along the collective reaction coordinate. (This is denoted % avg. change in Table 3.) For a random sampling of eighty distances, the standard deviation for this quantity was determined to be 7.4%. To determine the motions influencing the degree of dynamical barrier recrossing, we calculated the normalized weighted correlation between each geometrical property at the transition state and ξ , which indicates the degree of barrier recrossing. (This is denoted % dynam. correl. in Table 3.) For a random sampling of eighty distances, the standard deviation for this quantity was determined to be 10.5%.

We focused on the residues found to be conserved across 36 diverse species from *E. coli* to human, as indicated in Figure 1.¹³ To provide a complete study of these conserved residues, we investigated the following set of distances. For each residue, we considered the C_α , the C_β , and the non-hydrogen atom closest to the end of the side chain. We studied the distances between these atoms and the donor and acceptor carbon atoms, as well as the minimum distance between the non-hydrogen atom closest to the end of the side chain and both the substrate and coenzyme. We also studied the minimum distance between any non-hydrogen atom of each residue and both the substrate and coenzyme. Including several other distances of interest and accounting for redundancies in this scheme, we investigated a total of 211 distances. Table 3 includes only those distances exhibiting statistically meaningful values (i.e., for which there is less than 20% probability of obtaining this value according to a normal distribution with the standard deviations given above) for either the thermally averaged or dynamical quantities. (Note that 19 out of 25 conserved residues impact one or both of these quantities.) The other distances investigated are included in the Supporting Information.

TABLE 3: Statistics of Enzyme Motion

atom 1	atom 2	avg. dist. reactant ^a	avg. dist. TS ^b	% avg. change ^c	% dynam. correl. ^d
C _D	C _A	3.28	2.73	-16.64	17.49
ALA7-C _β	DHF-N3	3.53	3.68	4.39	-14.90
ILE14-C _α	C _A	8.94	8.76	-2.02	13.78
ILE14-C _δ	C _D	5.23	5.75	9.93	-13.93
ILE14-C _δ	NDP-NC2	4.33	4.85	12.03	-9.98
GLY15-C _α	C _A	9.45	9.04	-4.40	30.37
GLY15-C _α	DHF-N10	9.06	9.65	6.44	14.47
ASP27-O _{δ1}	C _D	9.27	7.95	-14.21	13.14
ASP27-O _{δ1}	NDP-NO7	6.80	5.42	-20.25	4.25
ASP27-O _{δ1}	DHF-NA2	2.91	3.82	31.30	4.68
ASP27-O _{δ2}	DHF-N3	2.92	3.53	20.92	-6.24
ASP27-O _{δ2}	NDP-NO7	5.70	6.69	17.32	-4.33
LEU28-C _α	C _A	7.87	8.64	9.83	-5.49
LEU28-C _{δ1}	C _A	7.74	9.13	17.87	2.10
LEU28-C _{δ1}	DHF-C	5.74	8.04	40.23	3.35
LEU28-C _{δ2}	DHF-OA4	4.20	3.44	-18.17	-12.30
LEU28-C _{δ2}	NDP-NO7	7.80	6.58	-15.63	-7.82
PHE31-C _α	C _A	7.32	8.15	11.30	-17.57
PHE31-C _β	C _A	6.04	6.89	14.08	-15.39
PHE31-C _{δ2}	DHF-O1	6.06	4.27	-29.46	22.15
PHE31-C _ξ	DHF-C11	5.97	4.95	-17.11	17.88
PHE31-C _ξ	C _A	4.10	4.88	19.04	-17.32
VAL40-C _α	C _A	9.98	10.07	0.89	-14.47
VAL40-C _β	C _A	9.03	8.94	-1.02	-13.88
VAL40-C _{γ1}	DHF-O1	11.48	9.05	-21.09	16.51
ILE41-C _δ	NDP-AN7	11.45	11.26	-1.65	-15.49
GLY43-C _α	C _A	10.73	10.60	-1.21	14.24
ARG44-C _α	C _A	12.71	12.20	-4.03	22.37
ARG44-C _β	C _A	14.15	13.64	-3.59	22.15
ARG44-NH1	C _A	17.83	16.83	-5.57	14.01
ARG44-NH1	DHF-C9	16.72	15.86	-5.14	15.12
ARG44-NH1	NDP-AO6*	4.68	5.32	13.64	-0.75
ARG44-NH2	NDP-AO8*	3.92	3.29	-15.91	-19.18
THR46-C _α	C _A	7.63	7.00	-8.18	32.62
THR46-C _β	C _A	6.83	6.31	-7.62	30.10
THR46-O _{γ1}	C _A	6.94	6.47	-6.77	20.64
THR46-C _{γ2}	DHF-C9	4.48	4.17	-6.98	19.25
TRP47-N	DHF-C9	7.61	7.06	-7.23	27.01
TRP47-C _α	C _A	9.65	8.95	-7.24	23.28
TRP47-C _β	C _A	10.83	10.21	-5.73	20.83
LEU54-C _{δ1}	C _A	9.34	10.16	8.87	-17.57
LEU54-C _{δ1}	C _D	12.10	12.70	4.94	-18.64
LEU54-C _{δ1}	DHF-C16	6.42	5.62	-12.49	-17.78
LEU54-C _{δ1}	NDP-NC5	12.12	12.82	5.81	-20.53
LEU54-C _{δ2}	DHF-CT	6.48	4.26	-34.28	-8.53
ILE61-C _δ	C _D	13.11	13.05	-0.50	-14.52
LEU62-O	NDP-AC1*	3.18	3.20	0.48	-14.47
LEU62-C _α	C _A	14.60	14.49	-0.78	13.61
LEU62-C _{δ1}	C _A	15.01	14.09	-6.13	14.44
LEU62-C _{δ1}	DHF-C7	14.15	13.18	-6.83	18.57
LEU62-C _{δ1}	NDP-AC5	4.89	4.41	-9.90	-20.60
SER63-O _γ	C _D	16.91	17.00	0.56	-15.90
TYR100-OH	C _A	4.96	5.47	10.27	-16.16
TYR100-OH	C _D	3.56	3.72	4.36	-20.67
TYR100-OH	DHF-N8	3.81	4.44	16.54	-8.07
THR113-C _α	C _A	10.87	11.06	1.73	-15.56
THR113-O _{γ1}	C _A	9.28	9.54	2.89	-17.29
THR113-O _{γ1}	DHF-NA2	3.51	3.68	4.87	-29.72
ASP122-N	GLY15-O	2.97	3.28	10.42	-23.55
ASP122-C _β	C _A	15.75	15.53	-1.42	22.67
ILE14-C _δ	TYR100-OH	5.46	5.07	-7.15	-19.65

^a The weighted average distance between atom 1 and atom 2 in the reactant region $-157.74 \leq \Lambda^{(q)} \leq -152.96$ kcal/mol. The weighted average for a quantity x is $\langle x \rangle_w$, as defined in eq 9. ^b The weighted average distance between atom 1 and atom 2 in the transition state region $-2.39 \leq \Lambda^{(q)} \leq 2.39$ kcal/mol. ^c $[(\text{avg. dist. TS}) - (\text{avg. dist. reactant})]/(\text{avg. dist. reactant})$. ^d $\langle (x - \langle x \rangle_w)(y - \langle y \rangle_w) \rangle_w / \langle (x - \langle x \rangle_w)^2 \rangle_w \langle (y - \langle y \rangle_w)^2 \rangle_w^{-1/2}$ for two quantities x and $y = \xi$.

Figure 6 illustrates the thermally averaged values along the collective reaction coordinate and several representative real-

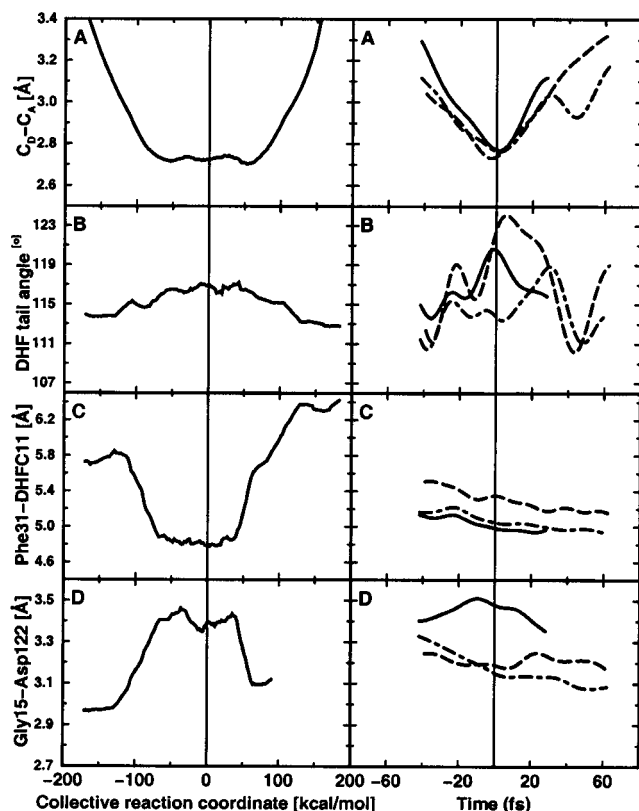


Figure 6. On the left are thermally averaged geometrical properties as functions of the collective reaction coordinate. On the right are representative real-time dynamical trajectories initiated at the transition state and propagated backward and forward in time. Note that the data on the left were presented in ref 13 but are included here for comparison. The properties shown are (a) the donor–acceptor distance, (b) the angle between the acceptor carbon and the methylene amino linkage in DHF, (c) the distance between C_α of Phe-31 and C11 of DHF, and (d) the hydrogen bond distance between Asp-122 and Gly-15.

time dynamical trajectories for four geometrical properties. These properties are the donor–acceptor distance, the angle between the acceptor carbon and the methylene amino linkage in DHF, the distance between C_α of Phe-31 and C11 of DHF, and the hydrogen bonding distance between Asp-122 and Gly-15. (Note that such hydrogen bonding motions are susceptible to sampling difficulties arising from metastable states in these simulations.) A comparison of the left and right sides of Figure 6 illustrates the difference between thermally averaged properties and real-time dynamical properties. The individual real-time trajectories reflect the conformations implicated in single molecule experiments.⁵⁵ This figure suggests that the donor–acceptor distance must decrease to ~ 2.7 Å at the transition state for the hydride transfer reaction, whereas the other promoting motions exhibit more variation. Note that the real-time trajectories on the right are on the femtosecond time scale, whereas the averaged properties on the left provide information about the millisecond time scale of the hydride transfer reaction. The overall mechanism and rate of catalysis are expected to be influenced more by motions occurring on the millisecond time scale than those on the femtosecond time scale. Nevertheless, the combination of both types of analyses provides insight into the detailed mechanism of the enzyme reaction.

The thermally averaged values in Figure 6 represent examples of motions participating in the network of coupled promoting motions described in ref 13. (Recall that promoting motions refer to systematic changes in thermally averaged geometrical properties as the reaction evolves from the reactant to the

transition state.) This figure indicates that the Phe-31 motion toward the substrate occurs simultaneously with the increase in the angle between the acceptor carbon and the methylene amino linkage in DHF, which in turn occurs simultaneously with the decrease in the donor–acceptor distance. Similarly, the motion of Gly-15 away from Asp-122 occurs simultaneously with the decrease in the donor–acceptor distance. Thus, the motions of Phe-31, Gly-15, and Asp-122 are coupled to the donor–acceptor motion and assist in the promotion of the hydride transfer reaction. We emphasize that this analysis is unable to differentiate between motions playing an active role in catalysis and motions responding to alterations caused by catalysis. Nevertheless, all of these systematic changes in thermally averaged properties occur along the same collective reaction coordinate representing hydride transfer.

The data in Table 3 provide a more complete characterization of the network of coupled promoting motions in DHFR. This table identifies the conserved residues that impact the activation free energy barrier, the dynamical barrier recrossings, or both. The thermally averaged motions influencing the activation free energy barrier occur on the millisecond time scale, whereas the dynamical motions influencing the barrier recrossings occur on the femtosecond to picosecond time scale. Although many of the residues in this network are in the active site, a number of these residues are on the exterior of the protein (i.e., Ser-63 and Asp-122). Thus, this network extends throughout the protein and involves motions on a wide range of time scales. Note that this network is most likely not complete or unique. Moreover, we emphasize that many of these conserved residues also play vital structural roles for binding the cofactor and substrate or for ensuring proper folding of the protein. These conserved residues may also play electrostatic roles in the enzyme reaction.

The catalytic importance of some residues in this network has been illustrated previously by mutagenesis experiments. Specifically, mutations of residues Asp-27, Leu-28, Phe-31, Arg-44, Leu-54, Tyr-100, Gly-121, Asp-122, and Thr-113 lead to a significant decrease in the rate of hydride transfer.^{1,56,57} Furthermore, double mutations of Leu-28 and Leu-54 exhibit strong nonadditivity, suggesting a coupling between these residues.^{3,4} (Note that this nonadditivity could be due to changes in structure.)

IV. Conclusions

This paper presented mixed quantum/classical molecular dynamics simulations of the hydride transfer reaction catalyzed by dihydrofolate reductase. The hybrid approach utilized in these studies includes nuclear quantum effects such as zero point energy and hydrogen tunneling, as well as the motion of the entire solvated enzyme, during the generation of the free energy profiles and the real-time dynamical trajectories. This approach allowed the calculation of rates and kinetic isotopes. It also provided insight into the fundamental nature of nuclear quantum effects, the physical basis for dynamical barrier recrossings, and the role of enzyme motion in catalysis.

The methodology used in these simulations was tested by comparison to experimental data and to an electronic structure calculation on a model system. The empirical valence bond potential was parametrized to reproduce the experimental free energies of activation and reaction.² The relevant geometrical properties of the reactive center at the transition state compared favorably to an electronic structure calculation for a model system. The excitation energies calculated from the hydrogen vibrational states for the reactant are similar to the local harmonic frequencies for the bending and stretching modes

of typical C–H bonds. Furthermore, the calculated deuterium kinetic isotope effect $k_{\text{dyn}}^{\text{H}}/k_{\text{dyn}}^{\text{D}} = 3.2 \pm 0.6$ agrees with the experimentally measured isotope effect of $k_{\text{exp}}^{\text{H}}/k_{\text{exp}}^{\text{D}} = 3.0 \pm 0.4$.² All of these results assist in the validation of the methodology used for these calculations.

The mixed quantum/classical simulations elucidated the significance of hydrogen tunneling in DHFR. Although the transferring hydrogen nucleus was represented by a three-dimensional vibrational wave function, the analysis of hydrogen tunneling was simplified by calculating one-dimensional hydrogen vibrational wave functions for a projected one-dimensional potential. This type of analysis was validated by the observation that the splittings between the lowest energy one-dimensional hydrogen vibrational states were similar to the splittings for the lowest energy three-dimensional vibrational states. A range of splittings between the lowest two hydrogen vibrational states were observed at the transition state. For the average splitting, the lowest one-dimensional vibrational state was ~ 1.1 kcal/mol below the one-dimensional barrier, implying the transmittal of probability through the barrier. The degree of hydrogen tunneling was found to be significantly greater than the degree of tunneling observed for liver alcohol dehydrogenase using similar methodology.

The transmission coefficient was found to be 0.80 for hydrogen and 0.85 for deuterium. The deviation of these transmission coefficients from unity indicates the significance of dynamical recrossings of the barrier. Most of the trajectories that exhibited recrossings crossed the barrier only one time in the forward direction and then quickly recrossed the barrier in the backward direction and returned to reactants. The barrier recrossings were found to be due mainly to insufficient flux at the transition state. Nonadiabatic transitions were more significant for deuterium than for hydrogen, but even for deuterium, the nonadiabatic transitions did not strongly impact the transmission coefficient. The transmission coefficients for DHFR are substantially lower than those calculated for liver alcohol dehydrogenase using similar methodology.

We investigated the impact of enzyme motions on the free energy of activation and the degree of barrier recrossing. The enzyme motions influencing the free energy barrier were determined by studying systematic changes in thermally averaged geometrical properties along a collective reaction coordinate as the reaction evolved from the reactant to the transition state. The enzyme motions influencing the degree of barrier recrossing were determined by studying the correlation between geometrical properties at the transition state and the degree of barrier recrossing for an ensemble of real-time dynamical trajectories initiated at the transition state. The thermally averaged motions occur on the millisecond time scale of the hydride transfer reaction, whereas the dynamical motions near the transition state occur on the femtosecond to picosecond time scale. We studied the motions of residues found to be conserved across 36 diverse species from *E. coli* to human.¹³ The data indicate that residues both in the active site and distal to the active site impact the free energy of reaction and the degree of barrier recrossing. Thus, we identified and characterized a network of coupled promoting motions that extends throughout the protein and involves motions on a wide range of time scales. This type of network may have evolved to optimize the hydride transfer step so that it is not the rate-limiting step in the overall enzyme reaction. Although this analysis focuses on the motions influencing the forward reaction, a similar analysis may be performed to study the motions influencing the backward reaction.

The concept of a network of coupled promoting motions has broad implications for protein engineering and drug design. Mutations may impact the rate of catalysis not only through alterations of the enzyme structure but also through the interruption of this network of coupled promoting motions. The present simulations provide an indication of the residues that participate in this network. Future simulations will center on studying the effects of single and multiple mutations of residues within this network.

Acknowledgment. We thank Dr. Simon Webb, Dr. Ravi Rajagopalan, and Dr. Stephen Benkovic for helpful discussions. We are grateful for financial support from NIH Grant GM56207 and NSF Grant CHE-0096357. S.H.-S. is the recipient of an Alfred P. Sloan Foundation Research Fellowship and a Camille Dreyfus Teacher-Scholar Award.

Supporting Information Available: Complete data from analysis of motions in DHFR. This material is available free of charge via the Internet at <http://pubs.acs.org>.

References and Notes

- (1) Miller, G. P.; Benkovic, S. J. *Chem. Biol.* **1998**, *5*, R105–R113.
- (2) Fierke, C. A.; Johnson, K. A.; Benkovic, S. J. *Biochemistry* **1987**, *26*, 4085.
- (3) Huang, Z.; Wagner, C. R.; Benkovic, S. J. *Biochemistry* **1994**, *33*, 11576.
- (4) Wagner, C. R.; Huang, Z.; Singleton, S. F.; Benkovic, S. J. *Biochemistry* **1995**, *34*, 15671.
- (5) Cummins, P. L.; Gready, J. E. *J. Comput. Chem.* **1998**, *19*, 977.
- (6) Cummins, P. L.; Gready, J. E. *J. Am. Chem. Soc.* **2001**, *123*, 3418.
- (7) Castillo, R.; Andres, J.; Moliner, V. *J. Am. Chem. Soc.* **1999**, *121*, 12140.
- (8) Sawaya, M. R.; Kraut, J. *Biochemistry* **1997**, *36*, 586.
- (9) Falzone, C. J.; Wright, P. E.; Benkovic, S. J. *Biochemistry* **1994**, *33*, 439.
- (10) Osborne, M. J.; Schnell, J.; Benkovic, S. J.; Dyson, H. J.; Wright, P. E. *Biochemistry* **2001**, *40*, 9846.
- (11) Radkiewicz, J. L.; Brooks, C. L. B., III. *J. Am. Chem. Soc.* **2000**, *122*, 225.
- (12) Mildvan, A. S.; Weber, D. J.; Kuliopulos, A. *Arch. Biochem. Biophys.* **1991**, *294*, 327.
- (13) Agarwal, P. K.; Billeter, S. R.; Rajagopalan, P. T. R.; Benkovic, S. J.; Hammes-Schiffer, S. *Proc. Nat. Acad. Sci.* (in press).
- (14) Billeter, S. R.; Webb, S. P.; Iordanov, T.; Agarwal, P. K.; Hammes-Schiffer, S. *J. Chem. Phys.* **2001**, *114*, 6925.
- (15) Billeter, S. R.; Webb, S. P.; Agarwal, P. K.; Iordanov, T.; Hammes-Schiffer, S. *J. Am. Chem. Soc.* **2001**, *123*, 11262.
- (16) Warshel, A. *Computer Modeling of Chemical Reactions in Enzymes and Solutions*; John Wiley: New York, 1991.
- (17) van Gunsteren, W. F.; Billeter, S. R.; Eising, A. A.; Hünenberger, P. H.; Krüger, P.; Mark, A. E.; Scott, W. R. P.; Tironi, I. G. *Biomolecular Simulation: The GROMOS96 Manual and User Guide*; Biomos b.v., Zürich and Groningen, VdF Hochschulverlag, ETH Zürich: Zürich, 1996.
- (18) Scott, A. P.; Radom, L. *J. Phys. Chem.* **1996**, *100*, 16502.
- (19) Frisch, M. J.; Trucks, G. W.; Schlegel, H. B.; Scuseria, G. E.; Robb, M. A.; Cheeseman, J. R.; Zakrzewski, V. G.; Montgomery, J. A., Jr.; Stratmann, R. E.; Burant, J. C.; Dapprich, S.; Millam, J. M.; Daniels, A. D.; Kudin, K. N.; Strain, M. C.; Farkas, O.; Tomasi, J.; Barone, V.; Cossi, M.; Cammi, R.; Mennucci, B.; Pomelli, C.; Adamo, C.; Clifford, S.; Ochterski, J.; Petersson, G. A.; Ayala, P. Y.; Cui, Q.; Morokuma, K.; Malick, D. K.; Rabuck, A. D.; Raghavachari, K.; Foresman, J. B.; Cioslowski, J.; Ortiz, J. V.; Stefanov, B. B.; Liu, G.; Liashenko, A.; Piskorz, P.; Komaromi, I.; Gomperts, R.; Martin, R. L.; Fox, D. J.; Keith, T.; Al-Laham, M. A.; Peng, C. Y.; Nanayakkara, A.; Gonzalez, C.; Challacombe, M.; Gill, P. M. W.; Johnson, B. G.; Chen, W.; Wong, M. W.; Andres, J. L.; Head-Gordon, M.; Replogle, E. S.; Pople, J. A. *Gaussian 98*, revision A.6; Gaussian, Inc.: Pittsburgh, PA, 1998.
- (20) Eisenberg, D.; Crothers, D. *Physical Chemistry with Application to the Life Sciences*; Benjamin/Cummings: Menlo Park, CA, 1979.
- (21) Scott, W. R. P.; Hünenberger, P. H.; Tironi, I. G.; Mark, A.; Billeter, S. R.; Fennen, J.; Torda, A. E.; Huber, T.; Kruger, P.; van Gunsteren, W. F. *J. Phys. Chem. A* **1999**, *103*, 3596.
- (22) Hammes-Schiffer, S.; Tully, J. C. *J. Chem. Phys.* **1994**, *101*, 4657.
- (23) Hammes-Schiffer, S. *J. Phys. Chem. A* **1998**, *102*, 10443.
- (24) Warshel, A.; Chu, Z. T. *J. Chem. Phys.* **1990**, *93*, 4003.

- (25) Laria, D.; Ciccotti, G.; Ferrario, M.; Kapral, R. *J. Chem. Phys.* **1992**, 97, 378.
- (26) Cao, J.; Voth, G. A. *J. Chem. Phys.* **1993**, 99, 10070.
- (27) Cao, J.; Voth, G. A. *J. Chem. Phys.* **1994**, 100, 5093.
- (28) Cao, J.; Voth, G. A. *J. Chem. Phys.* **1994**, 100, 5106.
- (29) Cao, J.; Voth, G. A. *J. Chem. Phys.* **1994**, 101, 6157.
- (30) Staib, A.; Borgis, D.; Hynes, J. T. *J. Chem. Phys.* **1995**, 102, 2487.
- (31) Billeter, S. R.; van Gunsteren, W. F. *Comput. Phys. Comm.* **1997**, 107, 61.
- (32) Tuckerman, M. E.; Marx, D.; Klein, M. L.; Parrinello, M. *Science* **1997**, 275, 817.
- (33) Bala, P.; Grochowski, P.; Nowinski, K.; Lesyng, B.; McCammon, J. A. *Biophys. J.* **2000**, 79, 1253.
- (34) Alhambra, C.; Corchado, J. C.; Sanchez, M. L.; Gao, J.; Truhlar, D. G. *J. Am. Chem. Soc.* **2000**, 122, 8197.
- (35) Villa, J.; Warshel, A. *J. Phys. Chem. B* **2001**, 105, 7887.
- (36) Antoniou, D.; Schwartz, S. D. *J. Phys. Chem. B* **2001**, 105, 5553.
- (37) Webb, S. P.; Hammes-Schiffer, S. *J. Chem. Phys.* **2000**, 113, 5214.
- (38) Iordanov, T.; Billeter, S. R.; Webb, S. P.; Hammes-Schiffer, S. *Chem. Phys. Lett* **2001**, 338, 389.
- (39) Wigner, E. *Phys. Rev.* **1932**, 40, 749.
- (40) Marcus, R. A. *Annu. Rev. Phys. Chem.* **1964**, 15, 155.
- (41) Zusman, L. D. *Chem. Phys.* **1980**, 49, 295.
- (42) Warshel, A. *J. Phys. Chem.* **1982**, 86, 2218.
- (43) King, G.; Warshel, A. *J. Chem. Phys.* **1990**, 93, 8682.
- (44) Ryckaert, J.-P.; Ciccotti, G.; Berendsen, H. J. C. *J. Comput. Phys.* **1977**, 23, 327.
- (45) Berendsen, H. J. C.; Postma, J. P. M.; van Gunsteren, W. F.; DiNola, A.; Haak, J. R. *J. Chem. Phys.* **1994**, 81, 3684.
- (46) Neria, E.; Karplus, M. *J. Chem. Phys.* **1996**, 105, 10812.
- (47) Tully, J. C. *J. Chem. Phys.* **1990**, 93, 1061.
- (48) Bennett, C. H. *Algorithms for Chemical Computation*; American Chemical Society: Washington, DC, 1997.
- (49) Keck, J. C. *J. Chem. Phys.* **1960**, 32, 1035.
- (50) Anderson, J. B. *J. Chem. Phys.* **1973**, 58, 4684.
- (51) Hammes-Schiffer, S.; Tully, J. C. *J. Chem. Phys.* **1995**, 103, 8528.
- (52) Allen, M. P.; Tildesley, D. J. *Computer Simulation of Liquids*; Clarendon Press: Oxford, U.K., 1989.
- (53) Andersen, H. C. *J. Comput. Phys.* **1983**, 52, 24.
- (54) Pretsch, E.; Seibl, J.; Clerc, T.; Simon, W. *Tables of Spectral Data for Structure Determination of Organic Compounds*, 2nd ed.; Springer-Verlag: Berlin, 1983.
- (55) Lu, H. P.; Xun, L.; Xie, S. *Science* **1988**, 282, 1877.
- (56) Cameron, C. E.; Benkovic, S. J. *Biochemistry* **1997**, 36, 15792.
- (57) Chen, J.-T.; Taira, K.; Tu, C.; Benkovic, S. J. *Biochemistry* **1994**, 33, 7021.